

See discussions, stats, and author profiles for this publication at: <https://www.researchgate.net/publication/231206902>

Photoelectrochemical Characterization of Nanocrystalline Thin-Film $\text{Cu}_2\text{ZnSnS}_4$ Photocathodes

ARTICLE in ACS APPLIED MATERIALS & INTERFACES · DECEMBER 2010

Impact Factor: 6.72 · DOI: 10.1021/am1008584

CITATIONS

63

READS

137

6 AUTHORS, INCLUDING:



Shannon C Riha

University of Wisconsin - Stevens Point

29 PUBLICATIONS 932 CITATIONS

SEE PROFILE



Justin Sambur

Cornell University

17 PUBLICATIONS 706 CITATIONS

SEE PROFILE



Amy L Prieto

Colorado State University

64 PUBLICATIONS 3,229 CITATIONS

SEE PROFILE



Bruce A Parkinson

University of Wyoming

251 PUBLICATIONS 6,959 CITATIONS

SEE PROFILE

Photoelectrochemical Characterization of Nanocrystalline Thin-Film $\text{Cu}_2\text{ZnSnS}_4$ Photocathodes

Shannon C. Riha,[†] Sarah J. Fredrick,[†] Justin B. Sambur,[†] Yuejiao Liu,[‡] Amy L. Prieto,^{*,†} and B. A. Parkinson^{*,‡}

Department of Chemistry, Colorado State University, Fort Collins, Colorado 80523, United States, and Department of Chemistry and School of Energy Resources, University of Wyoming, Laramie, Wyoming 82071, United States

ABSTRACT $\text{Cu}_2\text{ZnSnS}_4$ (CZTS) nanocrystals, synthesized by a hot injection solution method, have been fabricated into thin films by dip-casting onto fluorine doped tin oxide (FTO) substrates. The photoresponse of the CZTS nanocrystal films was evaluated using absorbance measurements along with photoelectrochemical methods in aqueous electrolytes. Photoelectrochemical characterization revealed a p-type photoresponse when the films were illuminated in an aqueous Eu^{3+} redox electrolyte. The effects of CZTS stoichiometry, film thickness, and low-temperature annealing on the photocurrents from front and back illumination suggest that the minority carrier diffusion and recombination at the back contact (via reaction of photogenerated holes with Eu^{2+} produced from photoreduction by minority carriers) are the main loss mechanisms in the cell. Low-temperature annealing resulted in significant increases in the photocurrents for films made from both Zn-rich and stoichiometric CZTS nanocrystals.

KEYWORDS: $\text{Cu}_2\text{ZnSnS}_4$ • thin films • solar cells • photoelectrochemistry • nano ink

INTRODUCTION

Interest in the development and commercialization of thin film solar cells has been growing over the past decade because of their low cost and scalability—two key factors needed to make solar technologies competitive with carbon-based fuels (1). Recent advances in CdTe and $\text{CuIn}_{1-x}\text{Ga}_x\text{Se}_2$ (CIGS) thin film solar cells have resulted in commercially viable photovoltaic modules (1–3). Despite having moderate efficiencies, CdTe and CIGS are not amenable for eventual terrawatt-scale production due to the cost and scarcity of Te, In, and Ga (2–4). Therefore, one major challenge of thin film technology is to develop materials composed of earth abundant and non-toxic elements that can be used to manufacture efficient photovoltaic devices.

$\text{Cu}_2\text{ZnSnS}_4$ (CZTS) is an emerging solar absorber that is structurally similar to CIGS, but contains only earth abundant, non-toxic elements and has a near optimal direct band gap energy of 1.4–1.6 eV and a large absorption coefficient of $\sim 1 \times 10^4 \text{ cm}^{-1}$ (4–6). Katagiri and co-workers have fabricated CZTS thin film solar cells by sputtering and vapor deposition techniques with efficiencies of up to 6.7 % (4, 7). However, these methods for thin film fabrication are costly, have low throughput, and can lead to inhomogeneous film composition (8). To reduce fabrication costs and overcome these drawbacks, many groups have employed other methods for thin-film solar cell fabrication such as spray pyrolysis

(9, 10), sol–gel sulfurization (11–14), electro- and photochemical deposition followed by sulfurization (2, 15), and liquid-precursor deposition (16). Kamoun and Kumar reported the spray pyrolysis of CZTS thin films using metal salts and thiourea precursors sprayed directly onto heated substrates (9, 10). Cu_xS impurities were found in films fabricated using various substrate temperatures and deposition times, while Kumar reported the films were Zn-rich and S-deficient. Uchiki and co-workers utilized a sol–gel method that involved spin-casting and drying CZTS precursor solutions containing metal salts, a solvent, and a stabilizer (11–14). After the sol–gel had been spin-cast onto the substrate, the precursor films were annealed in $\text{N}_2 + \text{H}_2\text{S}$ gas at 500 °C for 1 h. The resulting films contained near-stoichiometric CZTS; however, because of the high vapor pressure of sulfur, they were sulfur-deficient.

Another low-cost and scalable alternative to vacuum deposition is electrodeposition of the metals followed by a thermal reaction in sulfur vapor (15, 17–23). Scragg, et al. earlier reported the electrochemical deposition of metal layers where the film thickness was monitored by the charge passed (2). Films consisting of a 1 μm thick, three layer stack of Cu, Sn, and Zn were annealed at 550 °C in a quartz tube furnace for 2 h in a sulfur atmosphere. The authors reported that the films were predominately CZTS but had trace amounts of binary impurities such as SnS_2 and ZnS . In all cases the films were Zn-rich but the Zn composition varied across the film. Recently the authors reported using a rotating disk electrode and a Cu/Sn/Cu/Zn stack followed by sulfurization, which lead to a more uniform $\text{Cu}_2\text{ZnSnS}_4$ composition with small amounts of Cu_2S impurities, (21). Alternatively, Pawar, et al. reported a similar synthesis

* Corresponding author. E-mail: Bparkin1@uwyo.edu (B.A.P.);

Amy.Prieto@colostate.edu (A.L.P.).

Received for review September 9, 2010 and accepted December 6, 2010

[†] Colorado State University.

[‡] University of Wyoming.

DOI: 10.1021/am1008584

2011 American Chemical Society

method involving a single-step electrodeposition of all elements to eliminate the post sulfurization process. To obtain a crystalline sample, the authors reported annealing the films at 550 °C under Ar for 1 h (19). Although all of the above-mentioned methods offer a cost-effective and scalable alternative to vacuum deposition techniques of CZTS thin films, a majority of the techniques require additional annealing in a sulfur atmosphere at temperatures above 500 °C and the film stoichiometries obtained were not consistent and often contained binary and ternary impurity phases.

Recently Todorov, et al. reported a liquid processed, slurry-based coating method for fabricating high-performance solar cell devices of $\text{Cu}_2\text{ZnSn}(\text{S,Se})_4$ reaching 9.6 % efficiency without any H_2S processing step (24). Their process allowed for the in situ formation of CZT(S,Se) directly onto a conducting substrate simply by combining a slurry of Cu–Sn chalcogenides in hydrazine with Zn-chalcogenide precursors ($\text{ZnX}(\text{N}_2\text{H}_4)$ where $\text{X} = \text{S, Se, or Te}$). One drawback of this technique is that in order to crystallize the precursors into single-phase CZTS, the process required annealing at 540 °C, leaving minimal control over impurity phases. Fischereder et al. presented a similar method using solutions of metal salts and thioacetamide, which allowed for lower annealing temperatures (180–450 °C) (16). However, they could not rule out the presence of impurity phases in the lower-temperature-annealed samples.

To overcome the issues addressed above, a new method for scaling up solar cell production is based on nanocrystal “inks”, a printable solution of nanocrystals, which can either be thermally annealed into larger grain thin films or used as deposited to make solar cells using 3D arrays of photoactive nanocrystals (25, 26). The idea of having a printable ink has spurred interest in the synthesis of ternary nanocrystals such as $\text{CuIn}(\text{S,Se})_2$ for photovoltaics (27–29). Recently, our group (30), along with others (31–33), have reported the direct synthesis of quaternary CZTS and CZTSe using the hot injection method, a first step towards developing photoactive nanocrystal arrays from solution-processable inks (34). However, precise control over the solution phase synthesis (i.e. size, shape, doping concentration), characterization, and device fabrication of quaternary nanocrystals is in its infancy. It is therefore necessary to develop methods capable of quickly and effectively screening materials to optimize their syntheses. One way to do this is by using photoelectrochemical (PEC) techniques, which were used for the characterization of CZTS thin films by Scragg and Pawar (2, 19). In addition, Kameyama, et al. used PEC measurements to characterize layer-by-layer dipped CZTS nanocrystalline thin films (35). Herein, we report the fabrication and characterization of thin film photoelectrochemical photovoltaic cells in an aqueous electrolyte utilizing stoichiometric and Cu-poor/Zn-rich CZTS nanocrystal inks.

RESULTS AND DISCUSSION

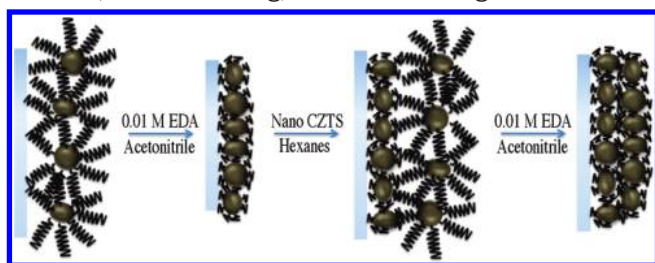
$\text{Cu}_2\text{ZnSnS}_4$ nanocrystals were synthesized using the hot injection solution synthesis method, which has been successful for the syntheses of a wide range of semiconducting chalcogenide nanocrystals, such as CdX ($\text{X} = \text{S, Se, Te}$) and CIGS (27, 29, 36, 37).

We chose this method because it not only provides control over composition and morphology, but also enables low-cost and scalable fabrication of solar cells through drop-casting, dip-coating, spin-coating, or printing the nanocrystals on an appropriate substrate (27, 29, 36, 38, 39). The hot injection method involves the injection of a cold solution of precursors into a hot surfactant solution, initiating the nucleation and growth of the nanocrystals (37, 40). The best reported CZTS photovoltaic conversion efficiencies were obtained when the material was Zn-rich (4, 7, 24); therefore, we synthesized CZTS samples that were near stoichiometric along with Zn-rich CZTS. The synthesis was carried out as previously described (30) with slight modifications presented in the Supporting Information. Briefly, appropriate amounts of copper(II) acetylacetonate, zinc acetate, and tin(IV) acetate were mixed under inert conditions in oleylamine (refer to Table S1 in the Supporting Information). In a separate vial, sulfur powder and oleylamine were sonicated until a red-orange solution was obtained. The reaction flask containing trioctylphosphine oxide (TOPO) was heated to 300 °C, followed by the simultaneous injection of the S and metal precursors. The reaction was quenched after 45 minutes by removing the product solution from the reaction flask and injecting minimal amounts of hexanes to prevent solidification when cooled to room temperature.

Analysis of the transmission electron microscopy (TEM) images of the resulting CZTS nanocrystals from the two reactions (stoichiometric versus Cu-poor/Zn-rich) showed that the CZTS particles exhibit both triangular and spherical morphologies with the spherical morphology being more abundant. (Figure S1 in the Supporting Information) The two different morphologies are consistent with the results of Guo, as well as Steinhagen, using similar synthesis procedures (31, 33). Size analysis reveals that the nanocrystals have similar average sizes of 10.3 ± 1.3 nm for the stoichiometric and 9.7 ± 1.3 nm for the Zn-rich composition (see Figure S1 in the Supporting Information).

To confirm the composition and structure of the CZTS nanocrystals, energy dispersive x-ray analysis (EDX) and x-ray diffraction (XRD) were performed on a solid sample of dried nanocrystals from each reaction. Compositional analysis from EDX reveals a near stoichiometric ratio of $\text{Cu}_{2.0}\text{Zn}_{1.0}\text{Sn}_{1.1}\text{S}_{3.9}$, whereas for the Cu-poor/Zn-rich sample, an average composition of $\text{Cu}_{1.9}\text{Zn}_{1.2}\text{Sn}_{1.0}\text{S}_{3.9}$ was determined. The XRD patterns (see Figure S2a in the Supporting Information) for stoichiometric and Zn-rich samples were indexed to tetragonal $\text{Cu}_2\text{ZnSnS}_4$ (JCPDS 26-0575, Figure S2b), and the average crystallite size, calculated by the Williamson–Hall method, was consistent with the particle size measured in the TEM images. No peaks consistent with Cu_xS or SnS_x were present in either pattern; however, it was not possible to rule out the presence of ZnS nor Cu_2SnS_3 impurities as their diffraction patterns contain peaks overlapping CZTS. A more in-depth analysis to confirm the phase purity of the CZTS nanocrystals can be found in our previous paper (30).

Scheme 1. Ligand Exchange Mechanism for the In Situ Replacement of Bulky Insulating Ligands (Introduced from the Synthetic Method) to a Short Chain (Less Insulating) Bifunctional Ligand



Thin films of CZTS nanocrystals, with thicknesses ranging from 50–650 nm, were prepared by a dip-casting procedure similar to that reported by Nozik and co-workers (34, 41). Glass slides with a 400 nm layer of fluorine-doped tin oxide (FTO) were used as a conducting substrate. The FTO substrates were mechanically dipped at a rate of 260 mm/min into a concentrated suspension of CZTS nanocrystals in a hexanes/toluene mixture, and then slowly removed from the suspension and allowed to dry. To remove the insulating TOPO capping ligands, we performed an in situ ligand exchange by dipping the substrate into a 0.01 M solution of ethylenediamine (EDA) in acetonitrile followed by slow removal and drying. The FTO substrate was then dipped back into the solution of nanocrystals and the process was repeated until a desired thickness was obtained. It has been shown that short chain ligands in acetonitrile will replace long chain ligands, which in turn decreases inter-nanocrystal spacing, Scheme 1, thereby facilitating the charge transfer through the nanocrystal film (42, 43). ATR-IR spectra taken of films prepared without ligand exchange show a stretch around 1140 cm^{-1} , corresponding to phosphine oxide (see Figure S3 in the Supporting Information). This suggests that the particles are TOPO-capped. The ATR data for the ligand exchanged films do not show this stretch. Rather, peaks were present at 1000 and 890 cm^{-1} corresponding to the νCN stretch and νNH bend of ethylenediamine (44). There is also an NH_2 stretch at 3200 cm^{-1} ; however, the resolution is low, making this a difficult stretch to observe. Overall, the IR data support the proposed ligand exchange mechanism in Scheme 1.

Figure 1 shows representative scanning electron microscopy (SEM) images of the surface and cross section of an as-prepared CZTS nanocrystal thin film. The top view image reveals that the nanocrystals are densely packed and distributed evenly throughout the entire surface of the film and that it is devoid of cracks. The cross-sectional image of a CZTS nanocrystal thin film dipped 20 times is shown in the inset of Figure 1 and shows that the film is approximately 125 nm thick. Considering the particles are ~ 10 nm in diameter, this implies that each successive dip resulted in submonolayer deposition of nanocrystals.

Optical absorbance measurements were also used to monitor the thickness of the nanocrystal films. Figure 2 (solid lines) displays the UV–vis spectra of as-deposited thin films from each reaction that were used to determine an absorp-

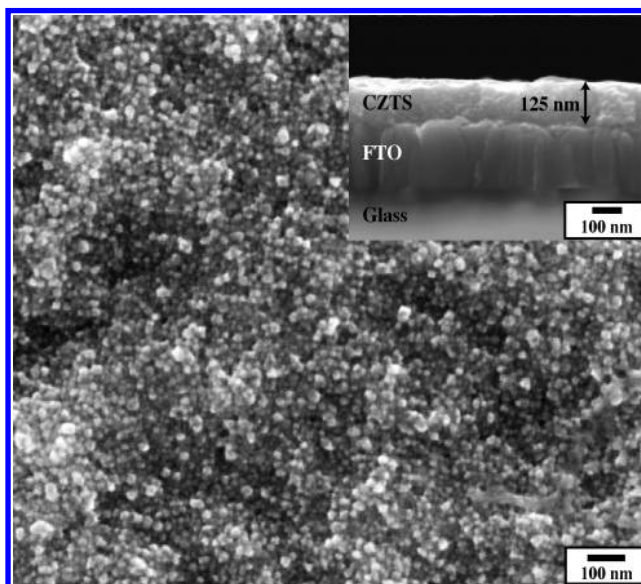


FIGURE 1. SEM image of a CZTS film prepared by dip-casting with an in situ ligand exchange to EDA. The top profile shows the CZTS nanocrystals are tightly packed. The inset is the side profile of the film.

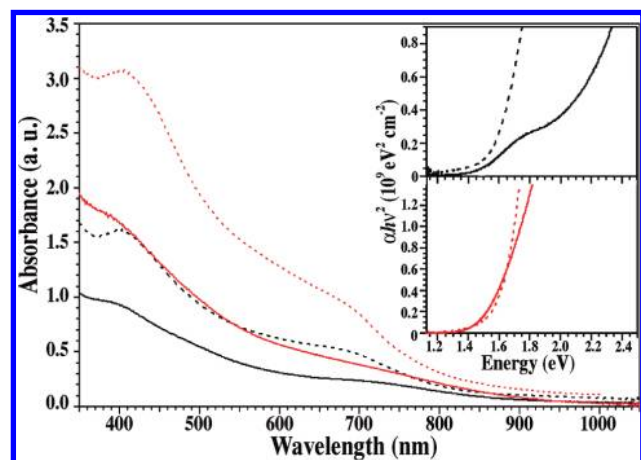


FIGURE 2. Optical absorption measurements of as-deposited (solid lines) and annealed (dashed lines) CZTS thin films. The black traces correspond to a 150 nm thick stoichiometric CZTS film and the red traces are for a 200 nm thick Zn-rich film. The absorption coefficient at the band gap is larger for the Zn-rich composition. Upon annealing, the band gaps slightly increase and become more direct.

tion coefficient. Extrapolating the linear portion of the plot $(\alpha h\nu)^2$ —the square of the absorption coefficient (α) multiplied by the photon energy ($h\nu$)—versus the photon energy yields direct band gaps of 1.45 and 1.52 eV for stoichiometric (black solid trace) and Zn-rich compositions (red solid trace), respectively. These values are consistent with literature values and are near optimal for solar conversion efficiency in a single junction device (4–6). Unpassivated nanocrystal surfaces have surface states that allow for transitions leading to the small absorption at sub-band gap energies. In addition, atomic disorder in the crystal structure can result in defect states that shift the band gap to lower energies, producing an indirect band gap not present in the ordered bulk crystal. One way to induce order within the nanocrystals is through annealing. Therefore, after dip casting, films were annealed under Ar in the presence of additional CZTS nanopowder at

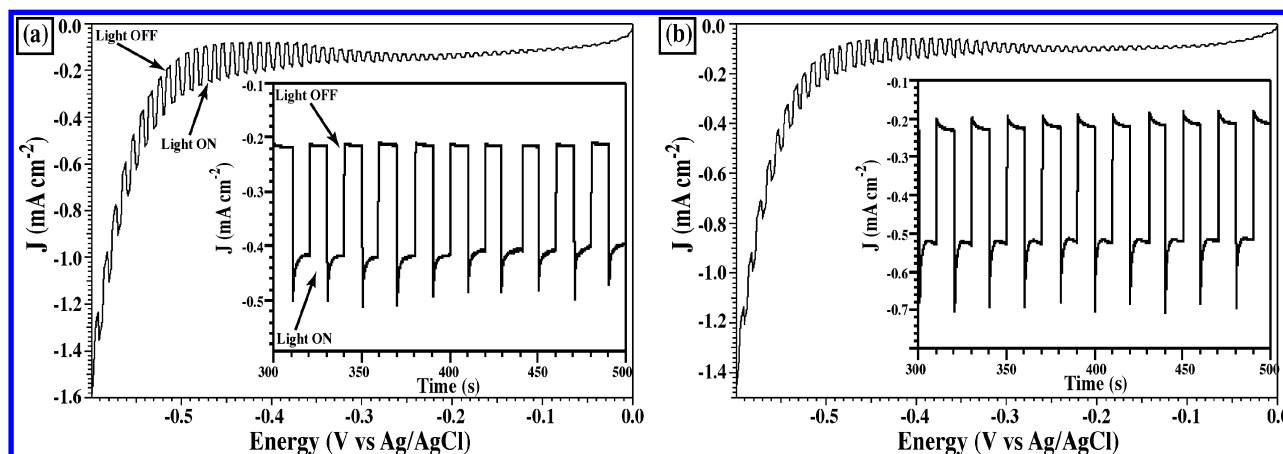


FIGURE 3. J - V plots of the photocurrent response of 205 nm thick, (a) stoichiometric and (b) Zn-rich, as-deposited CZTS nanocrystal thin films scanned cathodically from 0 to -600 mV vs Ag/AgCl at a scan rate of 2 mV/s using a 17 mW, 532 nm laser. The photocurrents increased with a more negative applied potential for both reactions. The insets are photostability measurements at -500 mV vs Ag/AgCl showing the photocurrent is quite stable at this potential. Both experiments were performed in a 0.1 M $\text{Eu}(\text{NO}_3)_3$ aqueous electrolyte.

350 °C (1000 Torr) for 1.5 h. The heat treatment, even though it is only 50 °C hotter than the synthesis temperature, drastically changed the absorbance of the CZTS films to have a much steeper onset or more like a direct transition (Figure 2, dashed lines). In addition, the band gap slightly increased to 1.56 and 1.59 eV for the stoichiometric and Zn-rich analogs, respectively. Possible explanations for these optical absorption changes are that low-temperature annealing leads to ordering within the nanocrystal, at a lower temperature than would be expected for macroscopic crystals, and that the annealing step leads to grain growth which reduces the number of sub-band gap surface states. We can test the hypothesis for grain growth with SEM and XRD. SEM images show that after annealing, the film thickness (see Figure S4 in the Supporting Information) decreases from about 440 nm to 340 nm or by about 20 %, indicating that the nanocrystals are more densely packed. In addition, Scherrer analysis of the X-ray diffraction patterns of an as-deposited film and a film annealed 1.5 h at 350 °C revealed an increase in average grain size from 12.7 ± 1.0 nm, consistent with the TEM results, to 47.8 ± 11.1 nm an almost 4-fold increase that may reduce the number of surface states (see Figure S5 in the Supporting Information). Therefore, the outcome of low-temperature annealing results in condensing the film and increases the grain size, reducing the number of grain boundaries and the surface area with potentially fewer surface states. It is also probable that annealing produced more ordering in the metal sublattice that would increase the density of states at the Γ point corresponding with the direct optical transition to account for the up to a factor of 10 increase in the optical absorption despite the same amount of CZTS material in the optical path length. Similar effects were observed when cation disorder was present in the chalcopyrite structure of ZnSnP_2 , resulting in an indirect band gap at lower energies rather than a direct gap in the ordered material (45).

We next investigated the photoresponse of the as-deposited films and compared them with the annealed thin films to determine if the improvements in absorption properties and changes in morphology lead to better photoelec-

trochemical properties. The nanocrystalline films, both as-dipped and annealed, were used as photoelectrodes in a three-electrode photoelectrochemical cell with a platinum mesh basket counter electrode and saturated Ag|AgCl reference electrode. The electrolyte contained aqueous 0.1 M KCl and 0.1 M $\text{Eu}(\text{III})(\text{NO}_3)_3$ which served as the redox mediator. The photocurrent, produced by illuminating the films with a chopped ~ 17 mW 532 nm green laser, was measured using a CH-Instruments potentiostat.

Photoelectrochemical characterization was chosen over preparing solid-state devices as it allows for a rapid, non-destructive evaluation of the CZTS thin films and eliminates electrical shorting from a vapor-deposited metal back contact penetrating through the pores in the film to the front contact. In addition, the conformal contact of electrolyte with the nanocrystals in the film minimizes the distance minority carriers (electrons) must diffuse to reduce the Eu^{3+} to Eu^{2+} before they can recombine with the photogenerated holes. The solution-based measurements allowed us to quickly test a variety of films in order to determine the optimal thickness and composition, as well as compare as-deposited and annealed films.

Figure 3a shows a current-voltage (J - V) curve of an as-deposited, stoichiometric, 205 nm thick CZTS nanocrystal thin film. The cathodic photocurrent increased gradually with increasing negative potential, indicating that the thin films were p-type (2). In a solid thin film, this would be attributed to an increase in the depletion layer thickness; however, the size of the nanocrystals cannot support a depletion layer because the space charge region is large compared to the particle size and the mobile ions in the electrolyte neutralize any electric field. The reduction potential of Eu^{3+} to Eu^{2+} is -550 mV vs Ag|AgCl, so we attribute the increase in dark current at potentials more negative than -550 mV to the reduction of Eu^{3+} to Eu^{2+} on the film and on the FTO substrate. For this reason, we focus on photocurrents produced at potentials more positive of -550 mV, where photogenerated carriers in CZTS are from the uphill reduction of Eu^{3+} .

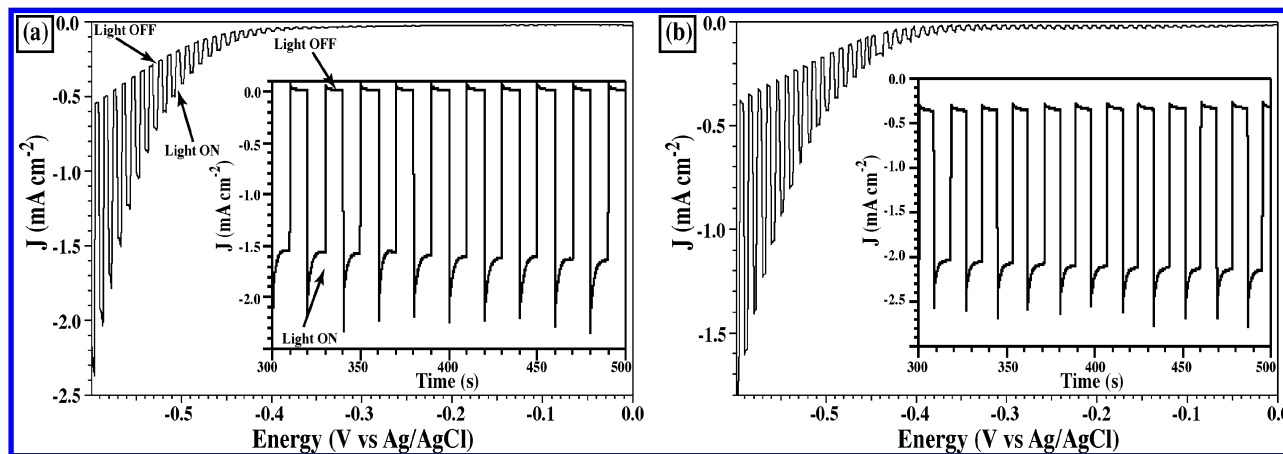


FIGURE 4. J - V plots of the photocurrent response from annealed, 150 nm thick CZTS nanocrystal thin films from (a) stoichiometric and (b) Zn-rich reactions, with the insets displaying the photostability measurements using a 0.1 M $\text{Eu}(\text{NO}_3)_3$ aqueous electrolyte. The dark current is reduced compared to the as-deposited films and the photocurrent density increases with a more negative applied potential. The annealed thin films both produced close to a 10-fold increase in the stable photocurrent density at -500 mV vs $\text{Ag}|\text{AgCl}$ under illumination from a 17 mW, 532 nm laser.

The stability of the photocurrent of an as-deposited thin film was evaluated at a constant potential of -500 mV by chopping the light with 10 sec on and 10 sec off, and the results are plotted in the inset of Figure 3a. The CZTS nanocrystal film showed a constant photocurrent-density of 0.19 mA cm^{-2} that remained stable over time despite being immersed in an aqueous electrolyte. Similar results were also obtained with thin films of the Cu-poor/Zn-rich CZTS nanocrystals as displayed in Figure 3b (as-deposited). This composition showed a slightly higher photocurrent-density response than the stoichiometric CZTS nanocrystals, consistent with current CZTS thin film literature (4, 7). The same photostability test (Figure 3b inset) showed a stable photocurrent-density of around 0.3 mA cm^{-2} .

As was previously displayed in the UV-vis spectra (Figure 2), annealing the CZTS nanocrystal thin films at 350°C leads to better absorption properties and a more direct band gap transition. Using as-deposited films, similar to those tested in Figure 3a, we annealed them at 350°C for 1.5 h under 1000 Torr of Ar. The film thickness for each sample decreased by about 20% (see Figure S4b in the Supporting Information). Figure 4a shows the JV curve of an annealed stoichiometric CZTS nanocrystal thin film, while Figure 4b displays the JV plot of an annealed Zn-rich CZTS nanocrystal thin film (220 nm) under illumination from a 17 mW, 532 nm laser. In comparison to the as-deposited films, the dark current is considerably reduced and the photocurrent density increases more rapidly. The SEM images show that the thin films became more condensed, resulting in the area of the exposed conducting substrate and dark current being reduced (see Figure S4 in the Supporting Information). The insets in panels a and b in Figure 4 again show the photostability tests for both sets of annealed thin films using the same 532 nm laser source. From the as-deposited to the annealed films, there is an almost 10-fold increase in photocurrent density to 1.65 and 1.8 mA cm^{-2} for both the stoichiometric and Cu-poor/Zn-rich CZTS reactions, respectively. All the chopped photocurrents show decay transients

indicative of recombination of photogenerated carriers through mechanisms that will be discussed below.

To study the effects of low-temperature annealing and stoichiometry on the spectral response of the films, we measured the incident photon to current efficiency (IPCE) spectra of the CZTS nanocrystal thin films at -0.35 V vs $\text{Ag}|\text{AgCl}$ in 0.05 M Eu^{3+} (pH 4). For comparison we show the results from the stoichiometric as-deposited film (black solid trace) and the Zn-rich as-deposited film (red solid trace) in Figure 5. The IPCE for the stoichiometric CZTS film is 1.8% at 500 nm, whereas the IPCE for the Zn-rich CZTS film is 2.8% at 500 nm. The increase in IPCE for the Zn-rich sample was consistent with the photocurrent measurements above, as well as with previous reports (6, 7, 20, 24). However, these values are rather low and do not exhibit a sharp onset of photoresponse when compared to those reported by Katagiri and Todorov for CZTS thin films (7, 24).

From Figure 5, it is clear that after annealing, the CZTS films of both the stoichiometric (dashed black curve) and the Zn-rich composition (dashed red curve) show a significantly enhanced photocurrent response. The onset of photocurrent is more pronounced with an overall increase of IPCE throughout the visible region for both annealed films but especially in the Zn-rich sample. In fact, at 500 nm the IPCE for the stoichiometric composition showed an increase from 1.8% to 3.1% after annealing, whereas the Zn-rich composition exhibited an over 3.5 times increase from 2.8 to 10.1%. On the basis of the UV-vis absorption spectra in Figure 2, the absorption coefficient for the Zn-rich sample are larger than those for the stoichiometric sample leading to better light absorption over all wavelengths.

Although annealing produced significant improvements in the photoresponse of the nanocrystal films, the values are less than those measured in polycrystalline thin film CZTS devices. Photocurrents in a photoconversion system depend on the separation of carriers in a space charge field, diffusion lengths, and recombination velocities of the photogenerated carriers (46). Because the nanocrystals are immersed in an

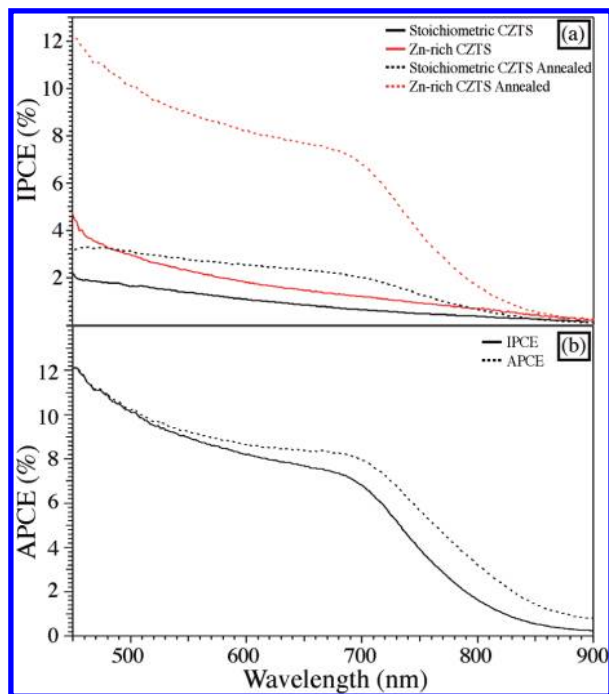


FIGURE 5. (a) IPCE measurements taken of as-deposited (solid) and annealed (dashed) stoichiometric CZTS films (black trace) and Zn-rich films (red trace). The measured IPCE mirrors the UV-vis and shows a more direct onset of IPCE for the annealed films. At 500 nm the IPCE for the stoichiometric film was 1.8 and 3.1% for as-deposited and annealed, respectively. The IPCE increased for the Zn-rich composition from 2.8% (as-deposited) to 10.1% (annealed film). (b) APCE values (dashed line) calculated from the IPCE and LHE values of an annealed Zn-rich CZTS film.

electrolyte containing mobile ions, a space charge field is not present, as it will be cancelled by the mobile ionic charges. Therefore, these devices should act much like the dye sensitized solar cell (DSSC), which operates on chemical potential gradients rather than electric field gradients. The majority carrier holes (whereas in a typical DSSC they are electrons) must diffuse through the nanocrystal network to be collected at the back FTO contact before they can recombine with a photogenerated electron or reoxidize Eu^{2+} in the electrolyte. The diffusion of carriers depends on the concentration gradients in the device as well as the number and energy distribution of recombination centers. The absorption profile of the incident light defines the concentration profile for the photogeneration of carriers and can be calculated by plotting $e^{-\alpha d}$, where α is the absorption coefficient, as a function of distance, d . The absorption profiles for our films calculated for three different wavelengths, 473, 532, and 632 nm, are shown in Figure 6 where the red curves are for the Zn-rich annealed films and the black curves represent the stoichiometric annealed films. The photocurrent in these devices, as in many thin film solar cells, is a trade off between absorbing all the light in a thicker film and collecting the majority carriers at the back contact via diffusion through the film. The majority carrier diffusion is particularly problematic in nanocrystal devices since they must traverse a tortuous path through many nanocrystals where interface states can act as recombination centers. Because the nanocrystal devices are porous and immersed in a redox electrolyte the collection of the minority carriers

should be relatively facile because they need to diffuse at most only half the distance of the nanocrystal diameter, less than 10 nm for the as-deposited films and between 15 and 25 nm for annealed film, to reduce a Eu^{3+} to Eu^{2+} .

We can estimate the diffusion length of holes by examining the absorbed photon to current efficiency (APCE), a function of the IPCE values for the 340 nm thick film. The APCE, shown in Figure 5b, is calculated by taking the IPCE and dividing it by the light harvesting efficiency (LHE), where LHE is equal to $1 - 10^{-\text{Abs}}$. In our case the best films have higher APCE values at all wavelengths beyond 550 nm and nearly identical APCE as IPCE values at lower wavelengths. According to the absorption profiles in Figure 6, at longer wavelengths of light, photogenerated charge carriers are produced throughout the film, requiring the holes to have much shorter diffusion lengths. On the contrary, based on the APCE value at 473 nm and Figure 6a, for front illumination, 80% of the light at this wavelength is absorbed and creates most of the charge carriers in the first 250 nm of the film. Therefore, most of the collected holes at the back contact must have diffused more than 100 nm, an impressive distance for such a disordered low-band-gap nanocrystal film. However, in comparison the electrons in a nanocrystalline TiO_2 cell can diffuse many micrometers.

To elucidate the role of carrier diffusion in these devices we measured IPCE spectra for both front illumination and back illumination (through the transparent substrate) in the redox electrolyte. Figure 7 shows a series of the front and back illumination IPCE spectra for the non-stoichiometric (Zn-rich) annealed film with film thicknesses ranging from 70 nm to 610 nm. The thinner 70, 95, and 125 nm thick films in Figure 7a–c, show only small differences in the shape of the IPCE spectra when illuminated from the back or the front but with an increase in the overall IPCE values as the films get thicker. The absorption profiles in Figure 6 reveal that a majority of the light still passes through the film resulting in a more uniform generation of carriers throughout the film and thus there is very little difference in the ability of the minority carriers to reach the back contact. However, once the film thickness increased to 340 nm (Figure 7d), there is a striking difference between front and back illumination. Longer wavelengths gave similar IPCE values for both front and back illumination but as the wavelength decreases, IPCE values for front illumination continued to increase, whereas for back illumination the IPCE values decreased more than an order of magnitude when compared to front illumination. A similar trend was also observed for a 610 nm thick film but with much smaller IPCE values at all wavelengths as shown in Figure 7e. Figure 8 summarizes IPCE values taken from plots a–e in Figure 7 at 473, 532, and 632 nm as a function of film thickness showing that as the film thickness increases the IPCE values produced from front illumination increased almost linearly up until a film thicknesses of 340 nm and then decreased for a thicker 610 nm film, whereas the back illumination IPCE values only increased until the film thickness reached

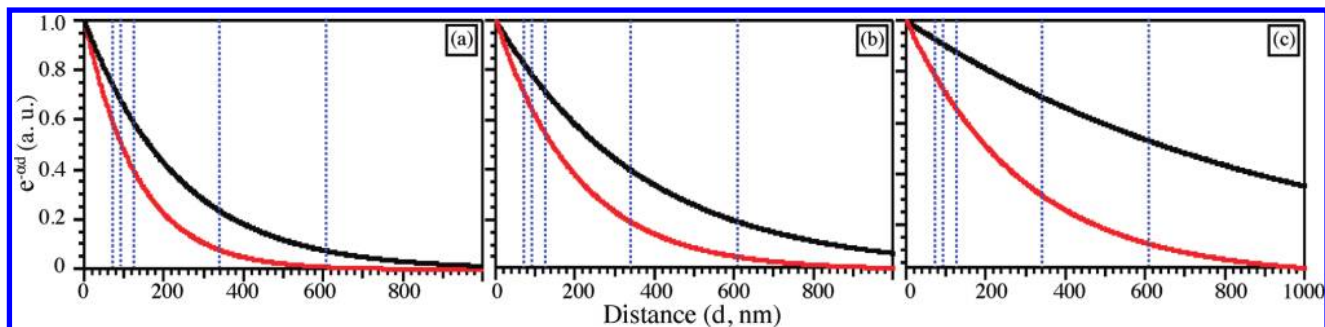


FIGURE 6. Absorption profiles calculated based on $\exp(-\alpha d)$, where α is the absorption coefficient for (a) 473 nm, (b) 532 nm, and (c) 632 nm and d is the distance. The red traces correspond to the Zn-rich annealed films, whereas the black traces are for the stoichiometric annealed films. Nearly 80% of the incident short wavelength light is absorbed in the first couple hundred nanometers of the film but as the wavelength increases, the light penetrates deeper into the films and more passes through the film. The blue traces indicate the various film thicknesses tested.

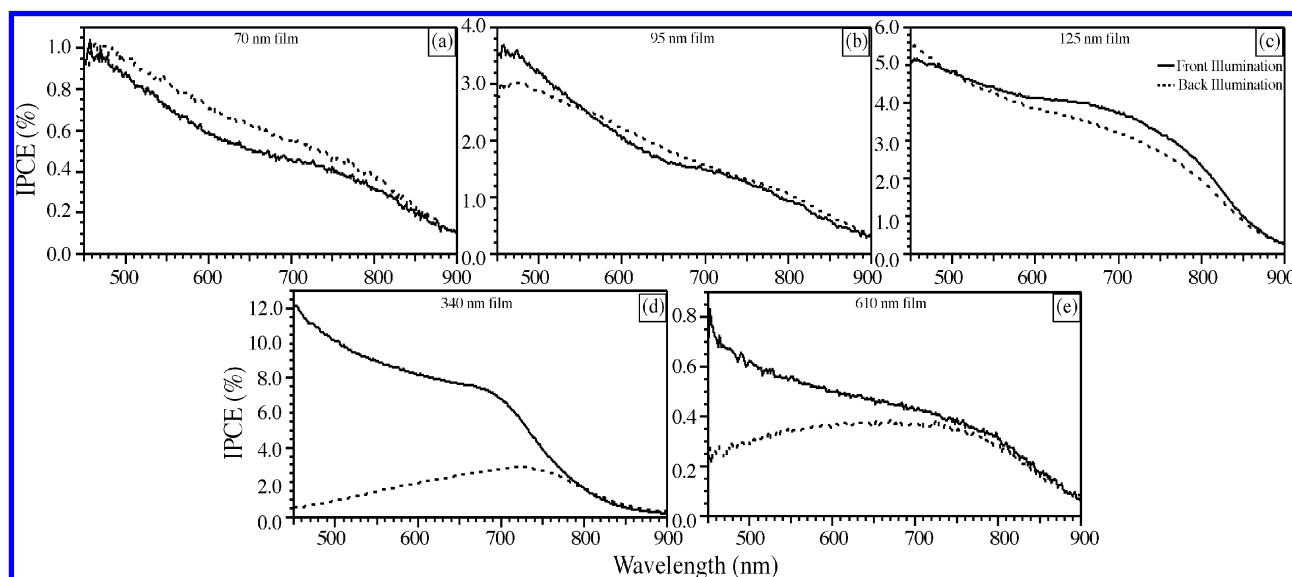


FIGURE 7. Photocurrent spectra recorded as a function of Zn-rich annealed films of various thickness with front and back illumination. The film thicknesses investigated were (a) 70, (b) 95, (c) 125, (d) 340, and (e) 610 nm.

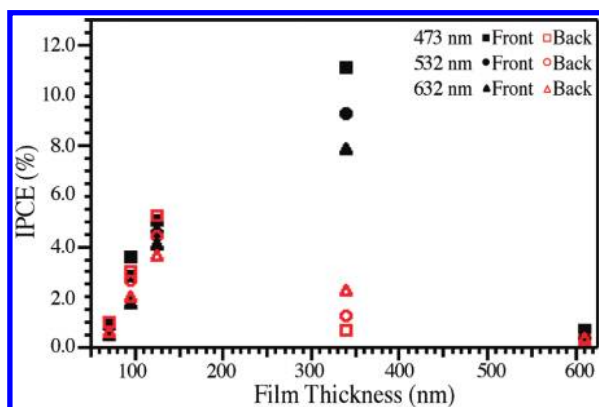


FIGURE 8. Plot of the IPCE values for both front (solid) and back (open) illumination at 473 nm (squares), 532 nm (circles), and 632 nm (triangles) wavelengths taken from the data in Figure 7. There is a general increase in front illuminated IPCE values with increasing film thickness up to 350 nm, after which the IPCE values significantly decrease. Back illumination IPCE values follow the same trend for films thinner than 125 nm, but as the film thickness increases, the IPCE values deviate substantially from those produced by front illumination.

125 nm and then decreased. At film thicknesses up to 125 nm, front and back illumination give similar IPCE values (47).

The absorption profiles in Figure 6 show that the majority (>80%) of the incoming light is absorbed when the film is thicker than 200 nm for 473 nm illumination, 260 nm for a 532 nm illumination, and almost 450 nm at 632 nm illumination. The greater light absorption in the thicker films produces both more total photogenerated carriers and a concentration gradient of carriers across the film, the direction of which is determined by the illumination direction. These trends can be understood by considering the absorption profiles shown in Figure 6. The thinner nanocrystal films will have low light absorption at all wavelengths resulting in nearly uniform generation of electron-hole pairs in the film with either front or back illumination and relatively small photocurrents. The redox couple can easily scavenge the small concentration of minority carriers, resulting in very low concentrations of reduced europium, and the holes have a relatively short distance to diffuse to the back FTO contact. As the films get thicker the majority of the electron-hole pairs are created near the front or back of the film depending on front or back illumination respectively, especially for the short wavelengths where the extinction coefficient is largest. The thicker films show nearly identical front and back

illumination IPCE values in their photoresponse spectra at wavelengths red of about 780 nm where the light is not strongly absorbed. The large decrease in photoresponse from back illumination in the blue region of the spectra is most likely due to recombination at the back contact. A large concentration of photogenerated electrons created near the back contact will produce a high concentration of Eu^{2+} near this contact. If the exchange current density for the usually slow electron transfer reaction of the $\text{Eu}^{3+}/\text{Eu}^{2+}$ couple is much faster on the FTO surface than on the CZTS surface then the holes that make it to the back contact will simply reoxidize the Eu^{2+} created from the photogenerated electrons. This usually slow electron transfer reaction must not have a high exchange current on semiconducting CZTS due to the low dark currents in pure Eu^{3+} solutions, especially considering the extremely high surface area of the nanocrystal films.

Kinetic discrimination of redox processes is similar to the DSSC where the TiO_2 surface has very slow kinetics for reduction of triiodide and the cells are very inefficient with faster redox couples such as ferrocene/ferrocenium or when fabricated on bare metal substrates. Indeed a much faster redox mediator, the reduction of cobaltacenium to cobaltacene (Co(III)/Co(II)), with our CZTS nanocrystal thin film produces very poor photoresponse because the holes will quickly reoxidize any cobaltacene that was produced by photoreduction (Figure S6). One way to improve the device efficiency by slowing the electron transfer reaction is by using a blocking layer on the back contact. Indeed, the DSSC efficiency is improved by coating the conducting oxide back contact with a thin layer of TiO_2 (48, 49). The addition of a thin blocking layer to the FTO surface, which has a low exchange current density for the $\text{Eu}^{3+}/\text{Eu}^{2+}$ couple, is currently under investigation to improve the photoresponse in our devices.

However, additional recombination processes in these films may be occurring as suggested by the low APCE values, calculated from the IPCE and LHE results, for the CZTS nanocrystal thin films. Some insight into these processes can come from the light-intensity (I_0) dependence of the photocurrent density (J) because at reasonable light intensities there is a linear relationship between these parameters. Because all the photocurrents in our CZTS films show a transient response that decays to a more steady state value (Figures 3 and 4), it is apparent that there is a fast recombination process that may not be associated with the time scale for carrier diffusion. The results of the intensity dependence of the steady-state photocurrent, measured 8 s after illumination in a 0.1 M Eu(III) electrolyte, for the 340 nm thick films at an applied bias of -500 mV vs Ag|AgCl are presented in Figure 9. In an ideal system the short-circuit, J_{sc} , scales linearly with I_0 ; however, Figure 9a shows that it is not linear in our devices. Figure 9b shows the same data plotted on a log–log scale where a linear dependence is observed with a slope of 0.75 ($R^2 = 0.999$). Recombination is often a second-order process, because it is dependent on both the concentration of electrons and holes, but in our

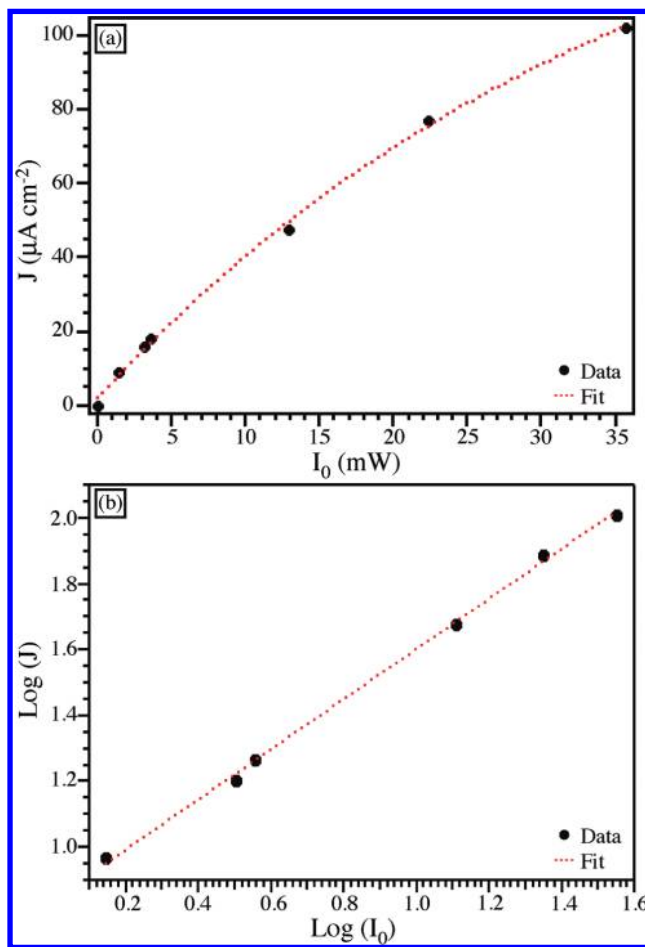


FIGURE 9. Steady-state photocurrent density, recorded 8 s after illumination from a 532 nm light source, as a function of light intensity at -500 mV vs Ag|AgCl . The data is plotted on (a) a linear scale and (b) in a log–log plot. The data in the log–log plot has a slope of 0.75 ($R^2 = 0.999$).

case, it may also be influenced by the diffusion of Eu^{3+} and Eu^{2+} that react with minority and majority carriers, respectively, resulting in a power dependence close to 0.75. Further investigation of the time, potential, and intensity dependence of the transient photocurrents will be necessary to elucidate the competing recombination pathways in these devices.

CONCLUSIONS

Stoichiometric and Cu-poor/Zn-rich CZTS nanocrystals have been synthesized using the hot-injection method. We have shown that CZTS nanocrystal thin films—fabricated by dip casting onto FTO substrates and ligand exchanged with ethylenediamine—immersed in a Eu^{3+} containing redox electrolyte, exhibit p-type photocurrents that increase with negative applied bias. The influence of film thickness and low-temperature annealing on the photocurrent response was studied on both stoichiometric and Zn-rich films. Low-temperature annealing of the as-deposited films at 350 °C for 1.5 h greatly improved the IPCE for both the stoichiometric and Zn-rich CZTS films from 1.8 to 3.1 % (stoichiometric) and 2.8 to 10.1 % (Zn-rich) at 500 nm, respectively. Although these photoconversion efficiencies are low in

comparison to the bulk counterparts, our studies were aimed at investigating the carrier transport processes in the semi-conducting nanocrystalline thin films. Optical absorbance measurements and photocurrent spectroscopy with both front and back illumination revealed that the CZTS nanocrystal thin films behave like a p-type version of the nanocrystalline TiO₂ scaffold in a dye-sensitized solar cell, and that a major loss mechanism in this cell is recombination via the redox couple at the back contact. This is due to oxidation of Eu²⁺ produced by the photogenerated electrons with the photogenerated holes diffusing to the back contact, which is due to the higher exchange current for this redox couple on FTO than on the surface of the CZTS nanocrystals.

Acknowledgment. We thank Dr. John Chandler and Dr. Gary Zito at the Colorado School of Mines (HR-TEM and SEM) for their assistance. Additional TEM imaging was supported in part by the Microscopy Imaging Network core infrastructure grant from Colorado State University. We thank the CSU Clean Energy Supercluster, the Center for Revolutionary Solar Photoconversion (CRSP), and DuPont for funding.

Supporting Information Available: Experimental details, additional TEM, ATR, and photocurrent measurements (PDF). This material is free of charge via the Internet at <http://pubs.acs.org>.

REFERENCES AND NOTES

- (1) Ginley, D.; Green, M. A.; Collins, R. *MRS Bull.* **2008**, *33*, 355.
- (2) Scragg, J. J.; Dale, P. J.; Peter, L. M.; Zoppi, G.; Forbes, I. *Phys. Status Solidi B* **2008**, *245*, 1772.
- (3) Wadia, C.; Alivisatos, A. P.; Kammen, D. M. *J. Environ. Sci. Technol.* **2009**, *43*, 2072.
- (4) Jimbo, K.; Kimura, R.; Kamimura, T.; Yamada, S.; Maw, W. S.; Araki, H.; Oishi, K.; Katagiri, H. *Thin Solid Films* **2007**, *515*, 5997.
- (5) Katagiri, H. *Thin Solid Films* **2005**, *480–481*, 426.
- (6) Katagiri, H.; Saitoh, K.; Washio, T.; Shinohara, H.; Kurumadani, T.; Miyajima, S. *Sol. Energy Mater. Sol. Cells* **2001**, *65*, 141.
- (7) Katagiri, H.; Jimbo, K.; Yamada, S.; Kamimura, T.; Maw, W. S.; Fukano, T.; Ito, T.; Motohiro, T. *Appl. Phys. Express* **2008**, *1*, 041201.
- (8) Tanaka, T.; Nagatomo, T.; Kawasaki, D.; Nishio, M.; Guo, Q.; Wakahara, A.; Yoshida, A.; Ogawa, H. *J. Phys. Chem. Solids* **2005**, *66*, 1978.
- (9) Kamoun, N.; Bouzouita, H.; Rezig, B. *Thin Solid Films* **2007**, *515*, 5949.
- (10) Kumar, Y. B. K.; Babu, G. S.; Bhaskar, P. U.; Raja, V. S. *Sol Energy Mater. Sol. Cells* **2009**, *93*, 1230.
- (11) Miyamoto, Y.; Tanaka, K.; Oonuki, M.; Moritake, N.; Uchiki, H. *Jpn. J. Appl. Phys.* **2008**, *47*, 596.
- (12) Tanaka, K.; Moritake, N.; Oonuki, M.; Uchiki, H. *Jpn. J. Appl. Phys.* **2008**, *47*, 598.
- (13) Tanaka, K.; Moritake, N.; Uchiki, H. *Sol. Energy Mater. Sol. Cells* **2007**, *91*, 1199.
- (14) Tanaka, K.; Oonuki, M.; Moritake, N.; Uchiki, H. *Sol. Energy Mater. Sol. Cells* **2009**, *93*, 583.
- (15) Moriya, K.; Watabe, J.; Tanaka, K.; Uchiki, H. *Phys. Status Solidi C* **2006**, *3*, 2848.
- (16) Fischereder, A.; Rath, T.; Haas, W.; Amenitsch, H.; Albering, J.; Meischler, D.; Larissegger, S.; Edler, M.; Saf, R.; Hofer, F.; Trimmel, G. *Chem. Mater.* **2010**, *22*, 3399.
- (17) Chan, C. P.; Chen, Z.; Lam, H.; Surya, C. *Proc. SPIE* **2009**, *7411*, 741108.
- (18) Ennaoui, A.; Lux-Steiner, M.; Weber, A.; Abou-Ras, D.; Kischau, I.; Schock, H. W.; Schurr, R.; Hlzing, A.; Jost, S.; Hock, R.; Vofsi, T.; Schulze, J.; Kirbs, A. *Thin Solid Films* **2009**, *517*, 2511.
- (19) Pawar, S. M.; Pawar, B. S.; Moholkar, A. V.; Choi, D. S.; Yun, J. H.; Moon, J. H.; Kolekar, S. S.; Kim, J. H. *Electrochim. Acta* **2010**, *55*, 4057.
- (20) Scragg, J. J.; Berg, D. M.; Dale, P. J. *J. Electroanal. Chem.* **2010**, *646*, 52.
- (21) Scragg, J. J.; Dale, P. J.; Peter, L. M. *Thin Solid Films* **2009**, *517*, 2481.
- (22) Zhang, X.; Shi, X.; Ye, W.; Ma, C.; Wang, C. *Appl. Phys. A* **2009**, *94*, 381.
- (23) Chan, C. P.; Lam, H.; Surya, C. *Sol. Energy Mater. Sol. Cells* **2010**, *94*, 207.
- (24) Todorov, T. K.; Reuter, K. B.; Mitzi, D. B. *Adv. Mater.* **2010**, *22*, E156.
- (25) Panthani, M. G.; Akhavan, V.; Goodfellow, B.; Schmidtke, J. P.; Dunn, L.; Dodabalapur, A.; Barbara, P. F.; Korgel, B. A. *J. Am. Chem. Soc.* **2008**, *130*, 16770.
- (26) Basol, B. M.; Kapur, V. K.; Norsworthy, G.; Halani, A.; Leidholm, C. R.; Roe, R. *Electrochem. Solid-State Lett.* **1998**, *1*, 252.
- (27) Koo, B.; Patel, R. N.; Korgel, B. A. *J. Am. Chem. Soc.* **2009**, *131*, 3134.
- (28) Koo, B.; Patel, R. N.; Korgel, B. A. *Chem. Mater.* **2009**, *21*, 1962.
- (29) Tang, J.; Hinds, S.; Kelley, S. O.; Sargent, E. H. *Chem. Mater.* **2008**, *20*, 6906.
- (30) Riha, S. C.; Parkinson, B. A.; Prieto, A. L. *J. Am. Chem. Soc.* **2009**, *131*, 12054.
- (31) Guo, Q.; Hillhouse, H. W.; Agrawal, R. J. *J. Am. Chem. Soc.* **2009**, *131*, 11672.
- (32) Shavel, A.; Arbiol, J.; Cabot, A. *J. Am. Chem. Soc.* **2010**, *132*, 4514.
- (33) Steinhagen, C.; Panthani, M. G.; Akhavan, V.; Goodfellow, B.; Koo, B.; Korgel, B. A. *J. Am. Chem. Soc.* **2009**, *131*, 12554.
- (34) Luther, J. M.; Law, M.; Beard, M. C.; Song, Q.; Reese, M. O.; Ellingson, R. J.; Nozik, A. J. *Nano Lett.* **2008**, *8*, 3488.
- (35) Kameyama, T.; Osaki, T.; Okazaki, K.-i.; Shibayama, T.; Kudo, A.; Kuwabata, S.; Torimoto, T. *J. Mater. Chem.* **2010**, *20*, 5319.
- (36) Peng, X. G.; Manna, L.; Yang, W. D.; Wickman, J.; Scher, E.; Kadavanich, A.; Alivisatos, A. P. *Nature* **2000**, *404*, 59.
- (37) Peng, Z. A.; Peng, X. J. *J. Am. Chem. Soc.* **2002**, *124*, 3343.
- (38) Cushing, B. L.; Kolesnichenko, V. L.; O'Connor, C. J. *Chem. Rev.* **2004**, *104*, 3893.
- (39) Milliron, D. J.; Hughes, S. M.; Cui, Y.; Manna, L.; Li, J.; Wang, L. W.; Alivisatos, A. P. *Nature* **2004**, *430*, 190.
- (40) Yin, Y.; Alivisatos, A. P. *Nature* **2004**, *437*, 664.
- (41) Liu, Y.; Gibbs, M.; Puthussery, J.; Gaik, S.; Ihly, R.; Hillhouse, H. W.; Law, M. *Nano Lett.* **2010**, *10*, 1960.
- (42) Luther, J. M.; Law, M.; Song, Q.; Perkins, C. L.; Beard, M. C.; Nozik, A. J. *ACS Nano* **2008**, *2*, 271.
- (43) Law, M.; Luther, J. M.; Song, Q.; Hughes, B. K.; Perkins, C. L.; Nozik, A. J. *J. Am. Chem. Soc.* **2008**, *130*, 5974.
- (44) Smith, B. *Infrared Spectral Interpretation: A Systematic Approach*; CRC Press: Boca Raton, FL, 1999.
- (45) Ryan, M. A.; Turner, J. A.; Williamson, D.; Peterson, M. W.; Frye, J. S.; Maciel, G. E.; Parkinson, B. A. *J. Mater. Res.* **1987**, *2*, 528.
- (46) Peter, L. M. *Chem. Rev.* **1990**, *90*, 753.
- (47) Films of each thickness were prepared and tested in triplicate from three different reaction batches of both stoichiometric and Zn-rich compositions. All sets showed similar trends between front and back illumination, in addition to the maximum current for films around 300 nm. However, the magnitude of the IPCE values or photocurrent was not consistent, therefore we did not show error bars in our figures.
- (48) Burke, A.; Ito, S.; Snaith, H.; Bach, U.; Kwiatkowski, J.; Gratzel, M. *Nano Lett.* **2008**, *8*, 977.
- (49) Yu, H.; Zhang, S.; Zhao, H.; Will, G.; Liu, P. *Electrochim. Acta* **2009**, *54*, 1319.

AM1008584